THE ASTRONOMICAL JOURNAL, 118:785–796, 1999 August

DUST PROPERTIES OF NGC 4753

G. C. DEWANGAN,[1] K. P. SINGH,[2] AND P. N. BHAT[3]
Department of Astronomy and Astrophysics, Tata Institute of Fundamental Research, Homi Bhabha Road, Mumbai 400005, India
Received 1999 January 7; accepted 1999 May 11

ABSTRACT

We report on *BVR* surface photometry of a lenticular galaxy, NGC 4753, with prominent dust lanes. We have used the multicolor broadband photometry to study dust extinction as a function of wavelength and derived the extinction curve. We find the extinction curve of NGC 4753 to be similar to the Galactic extinction curve in the visible region, which implies that the sizes of dust grains responsible for optical extinction are similar to those in our Galaxy. We derive the dust mass from optical extinction as well as from the far-infrared fluxes observed with *IRAS*. The ratio of the two dust masses, $M_{d,\mathrm{IRAS}}/M_{d,\mathrm{optical}}$, is 2.28 for NGC 4753, which is significantly lower than the value of 8.4 ± 1.3 found previously for a large sample of elliptical galaxies. The total mass of the observed dust within NGC 4753 is about a factor of 10 higher than the mass of dust expected from loss of mass from red giant stars and destruction by sputtering and grain-grain collisions in low-velocity shocks and sputtering in supernova-driven blast waves. We find evidence for the coexistence of dust and Hα-emitting gas within NGC 4753. The current star formation rate of NGC 4753, averaged over the past 2×10^6 yr, is estimated to be less than 0.21 $M_\odot$ yr^{-1}. A substantial amount of dust within NGC 4753 exists in the form of cirrus.

Key words: dust, extinction — galaxies: elliptical and lenticular, cD — galaxies: ISM — galaxies: photometry — infrared: galaxies

1. INTRODUCTION

It has now been well established that the presence of dust in early-type galaxies is the rule rather than an exception. Cool interstellar dust has been observed by *IRAS* (Jura 1986) and by means of optical extinction (Hawarden et al. 1981; Sadler & Gerhard 1985; Ebneter, Djorgovski, & Davis 1988; Goudfrooij et al. 1994b). Using *IRAS* data, Knapp et al. (1989) have shown that about 45% of the ellipticals and 68% of the S0 galaxies have been detected at the 60 and 100 μm bands, whereas Goudfrooij & de Jong (1995) have reported a detection rate of 61% for their sample of Shapley-Ames elliptical galaxies. The *Hubble Space Telescope* (*HST*) survey of ellipticals in the Virgo Cluster has revealed the presence of dust in the nuclei of almost every galaxy (Jaffe et al. 1994).

Apart from dust, early-type galaxies also contain substantial amounts of gas at various temperatures. Cold gas ($T \leq 100$ K) has been observed via its H I 21 cm line emission (Knapp, Turner, & Cunniffer 1985) and CO line emission (Wiklind & Rydbeck 1986; Phillips et al. 1986), warm gas ($T \approx 10^4$ K) via optical emission lines (e.g., [O II], [O III]; Caldwell 1984; Phillips et al. 1986), and hot gas via their X-ray emission (Forman, Jones, & Tucker 1985; Canizares, Fabbiano, & Trinchieri 1987; Fabbiano, Kim, & Trinchieri 1992). The interstellar medium (ISM) of early-type galaxies thus contains many different phases from cold to very hot. Typically they contain an amount of cool dust of mass $\simeq 10^4$–10^6 $M_\odot$ (Jura et al. 1987; Goudfrooij et al. 1994c), hot gas of mass $\simeq 10^9$–10^{10} $M_\odot$ (Forman et al. 1985; Fabbiano et al. 1992), and small amounts of warm gas of mass $\simeq 10^3$–10^5 $M_\odot$ (Phillips et al. 1986; Caldwell 1984).

The study of properties of different phases of ISM in early-type galaxies provides important clues to the origin, nature, and fate of the interstellar matter. In particular, dusty early-type galaxies provide a suitable environment to study the nature of extragalactic dust grains, either via their far-infrared (FIR) emission or optical extinction. The data can be used to study the physical mechanism operating on them, which can determine, among other things, their size distribution, temperature, abundances, formation, and destruction. The physical properties of the dust grains are functions of time and can be used as an indicator for the time elapsed since the dust was last substantially replenished (see Goudfrooij et al. 1994c).

The emission-line regions in X-ray–bright early-type galaxies are expected to be dust-free in view of very short lifetime ($\simeq 10^6$–10^7 yr) of dust grains. However, Goudfrooij et al. (1994c) found that the emission-line regions in these galaxies are essentially always associated with substantial dust extinction. This dilemma can be resolved in the evaporative flow scenario (de Jong et al. 1990) in which the observed dust immersed in hot, high-pressure plasma may be replenished by the evaporation of cool clouds. The presence of cool clouds is assumed to be due to the capture of a companion dwarf galaxy rich in dust and gas. A recent study of nuclear dust in 64 elliptical galaxies imaged with *HST* has shown that the dust and gas are generally dynamically decoupled (Van Dokkum & Franx 1995). Moreover, the kinematics of stars and gas in ellipticals with large dust lanes are found to be decoupled (e.g., Bertola et al. 1988). These conclusions generally indicate an external origin of dust in these galaxies. Further, the dynamical state of dust and gas can be used to probe the intrinsic shape of the underlying galaxy. The dust and gas, settled in the galaxy potential, are allowed in stable closed orbits, which indicates a plane in the galaxy (Merritt & de Zeeuw 1983; Habe & Ikewchi 1985, 1988).

[1] gulab@tifr.res.in.
[2] singh@tifr.res.in.
[3] pnbhat@tifr.res.in.

TABLE 1

BASIC PARAMETERS OF NGC 4753

Parameter	Value
α (J2000)	$12^h52^m23\overset{s}{.}23$
δ (J2000)	$-01°12'00\overset{''}{.}50$
Distance	8.7 Mpc
Velocity	1225 km s^{-1}
Magnitude	$U_T = 11.26 \pm 0.10$; $B_T = 10.85 \pm 0.10$; V (Johnson) = 10.30
FIR flux densities (mJy)	$f(12\ \mu m) = 340 \pm 42$; $f(25\ \mu m) = 310 \pm 71$; $f(60\ \mu m) = 2640 \pm 60$; $f(100\ \mu m) = 8010 \pm 176$

In this paper, we present a detailed study of dust properties of an early-type galaxy, NGC 4753, with very prominent dust lanes. NGC 4753 is located at a distance of 8.7 Mpc, as determined from a distance modulus of 29.7 by Buta et al. (1985) using published estimates and the light curve of supernova SN 1983g observed within the galaxy. NGC 4753 has been classified as a peculiar S0-type galaxy in the Hubble atlas (Sandage 1961) because its underlying luminosity distribution resembles an S0-type galaxy. However, the Third Reference Catalogue (RC3; de Vaucouleurs et al. 1991) classifies it as an irregular type, I0. The complex dust lanes in NGC 4753 pass through its center. Steiman-Cameron, Kormendy, & Durisen (1992) have shown using R-band photometry that the dust lanes lie in a disk that is strongly twisted by differential precession. We have carried out BVR surface photometry of NGC 4753 and derived its color and extinction maps. Based on these, we estimate the dust-mass from optical extinction. We have also derived the dust mass based on FIR emission. The observed optical (RC3) and IR (Knapp et al. 1989) properties of NGC 4753 are summarized in Table 1. The paper is organized as follows. In the next section we provide details of our observation. In § 3 we present our method of analysis and the results obtained. In § 4 we discuss our results, followed by conclusions in § 5.

2. OBSERVATIONS

NGC 4753 was observed with the Vainu Bappu Telescope (VBT) on the night of 1996 March 13. The observations were carried with a liquid nitrogen–cooled TEK 1024 × 1024 CCD chip placed at the prime focus of the 2.3 m reflector. The nominal value of the f-ratio is f/3.25. The pixel size of 24 μm^2 pixel^{-1} of the CCD chip gives a scale of $0\overset{''}{.}6$ pixel^{-1} and a total field of $10\overset{'}{.}24 \times 10\overset{'}{.}24$. The observations were carried out under photometric conditions. The seeing (FWHM) was in the range $2\overset{''}{.}1$–$2\overset{''}{.}6$. The exposure times were chosen not to saturate the CCD pixels because of the presence of bright stars in the neighborhood of the galaxy NGC 4753. In order to achieve a good signal-to-noise ratio, two images of NGC 4753 were taken in each of the broadband filters B, V, and R, with exposure times 300, 180, and 60 s, respectively. To correct for the bias level, bias images were taken just before and after the galaxy observation apart from many bias frames taken during the observing night. Several flat-field images in each filter were taken by exposing to the twilight and dawn sky in order to correct for the nonuniformity of response of pixels of the CCD. The standard star field in the "dipper asterism" region of the open cluster M67 was observed for photometric calibration. Both NGC 4753 and M67 were observed close to the zenith.

3. ANALYSIS AND RESULTS

We have used an IRAF[4] software package for the basic reduction and analysis of CCD images. Examination of the bias frames showed that the mean bias level did not vary significantly over the observation run. An average bias frame, constructed from bias frames taken very close to the galaxy observation, was subtracted from each of the object frames and flat-field frames. The bias-subtracted frames were trimmed to a size of 700 × 850 pixels in order to avoid the effects due to vignetting at the edges. The pixel-to-pixel response variation in each of the object frames were corrected by dividing the object frames by master flat frames in each band separately. The master flat frame in a filter band was obtained by averaging the best flat frames in the same filter and normalizing by the mean intensity level of the averaged frame. Cosmic-ray events, seen as few isolated bright pixels, were removed by replacing them by the average intensity of four nearest neighbors. The two frames of NGC 4753, obtained in each band, were combined after alignment, which increased the signal-to-noise ratio. The point-spread functions of individual and combined frames in each band were found to be similar to an accuracy better than 0.5%, which implies that the alignments were correct. The pixel coordinates in each of the object images were converted into the standard equatorial coordinates for the epoch J2000.0. The plate solutions were computed by fitting a quadratic polynomial between the known celestial coordinates and pixels coordinates of stars nearby to the object after projecting the celestial coordinates onto the plane tangent to the object center. The subsequent analysis utilized the final corrected and combined object images. The bias-corrected and flat-fielded B- and R-band images of NGC 4753 are shown in Figures 1 and 2, respectively, where the effect of extinction due to dust can easily be seen as the severe departure of the isophotes from the nearly elliptical shapes at the positions of dust lanes or patches. It is also clear that the extinction due to dust is larger in the B band, compared with that in the R band.

3.1. *Photometric Calibration*

Many authors (e.g., Chevalier & Ilovaisky 1991; Mayya 1991; Anupama et al. 1994; Bhat et al. 1992) have emphasized the advantages of using the standard star field in the "dipper asterism" region of the open cluster M67 for photometric calibration. We have determined instrumental magnitude of stars in the "dipper asterism" region of M67

[4] IRAF is distributed by the National Optical Astronomy Observatories, which are operated by the Association of Universities for Research in Astronomy, Inc. under cooperative agreement with the National Science Foundation. The IRAF version 2.11.1 was used.

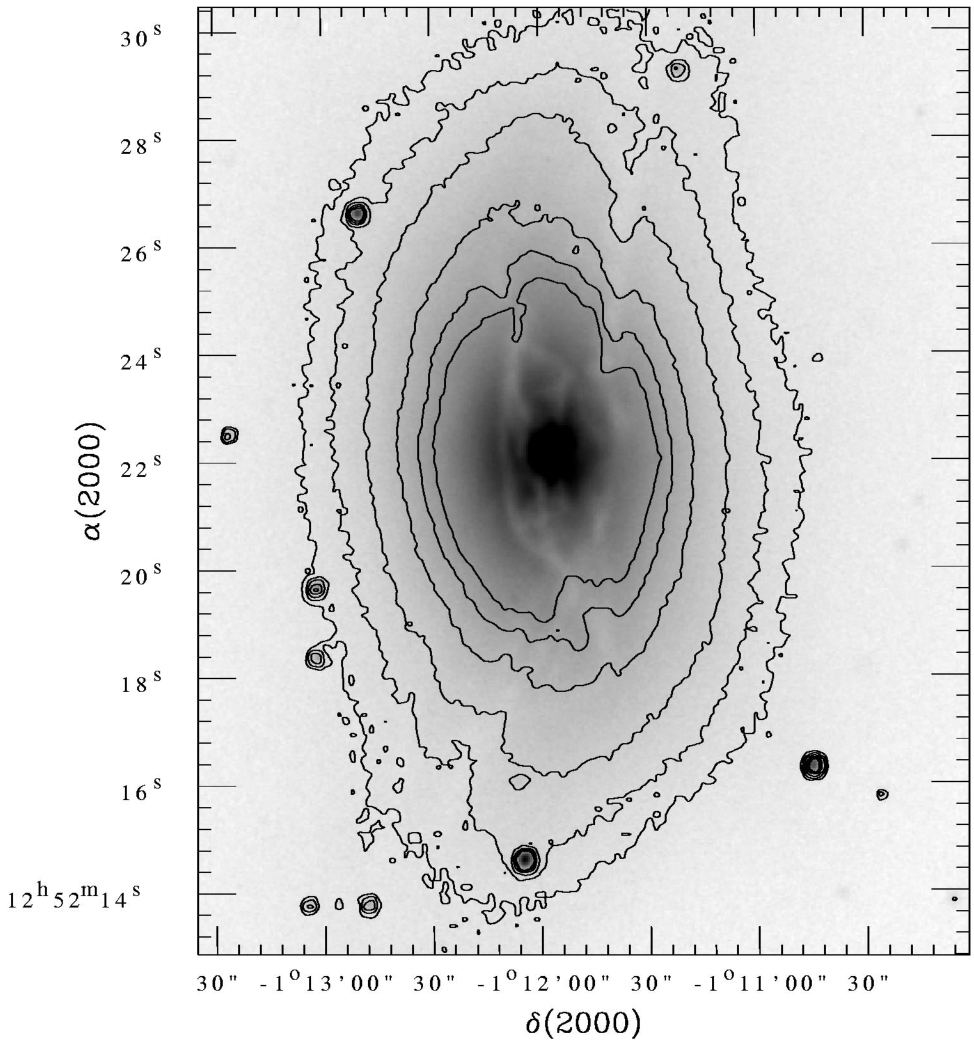

FIG. 1.—Bias-subtracted, flat-fielded and cosmic-ray–removed *B*-band image of NGC 4753, superposed on which are the contours of same image. The contour levels are drawn at 4.2%, 4.5%, 5%, 6%, 7%, and 8% of the peak intensity. The outermost contour is drawn at a surface brightness 23.1 mag arcsec^{-2}. The brighter lanes or patches represent dust-occupied regions.

by profile-fitting photometry using the DAOPHOT routine within IRAF. The method is discussed in detail by Stetson (1987). To correct the instrumental magnitudes for atmospheric extinction, we have made use of extinction coefficients given by Mayya (1991), who, based on eight nights observation at VBT during 1991 January–April, has determined the average extinction coefficients for the observatory. The extinction-corrected instrumental magnitudes and colors were transformed into the standard *BVR* system by fitting the following equations to the data:

$$V - v_0 = \alpha_v + \beta_v(B-V) , \quad (1)$$

$$B-V = \alpha_{b-v} + \beta_{b-v}(b-v)_0 , \quad (2)$$

$$V-R = \alpha_{v-r} + \beta_{v-r}(v-r)_0 , \quad (3)$$

$$B-R = \alpha_{b-r} + \beta_{b-r}(b-r)_0 , \quad (4)$$

where the uppercase letters *B*, *V*, and *R* are the standard magnitudes in the corresponding filters, taken from Chevalier & Ilovaisky (1991). The linear regression model chosen to fit the data was an ordinary least-squares regression of y on x [OLS(Y|X)], which has been recommended for the data used for calibration purposes (see Isobe et al. 1990; Feigelson & Babu 1992). The derived transformation coefficients are given in Table 2.

3.2. *Surface Photometry*

We have carried out isophotal analysis of the galaxy NGC 4753 in the *B*, *V*, and *R* bands. The shapes of the isophotes were analyzed using the ellipse-fitting routine within the STSDAS[5] software package (for details, see Jedrzejewski 1987). A proper background subtraction is crucial in the analysis. We determined the median intensity level

TABLE 2

TRANSFORMATION COEFFICIENTS

Quantity	α	β
$V - v_0$	0.399 ± 0.004	0.021 ± 0.006
$B-V$	−0.473 ± 0.015	1.416 ± 0.018
$V-R$	−0.041 ± 0.008	1.001 ± 0.017
$B-R$	−0.482 ± 0.008	1.248 ± 0.006

[5] STSDAS is distributed by Space Telescope Science Institute; version 2.0.1 was used.

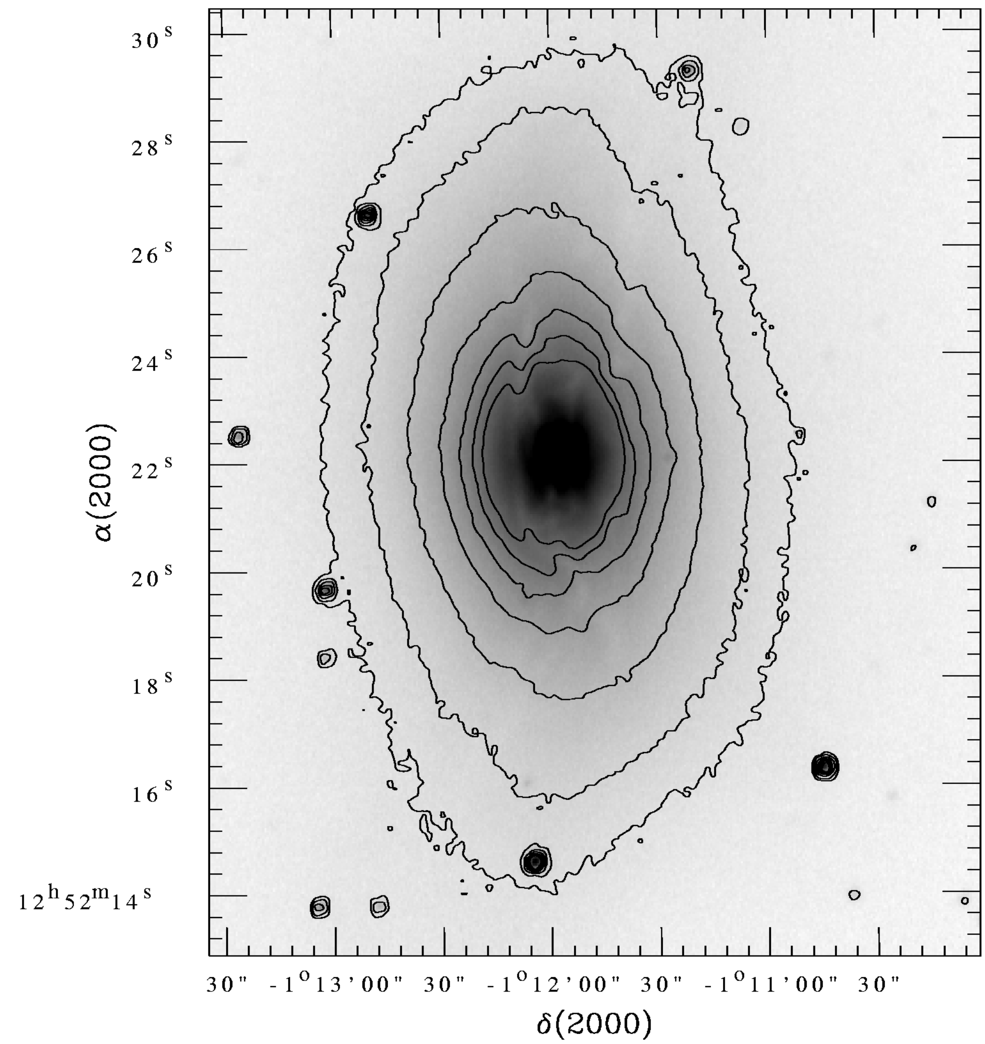

FIG. 2.—*R*-band image of NGC 4753 overlapped with the contours of the same image. The contour levels are drawn at 3%, 3.3%, 4%, 5%, 6%, 7%, and 8% of the peak intensity. The outermost contour corresponds to the surface brightness 22.1 mag arcsec^{-2}.

(and its associated dispersion) in several 25 × 25 pixel boxes in the source-free regions of an object image. The dispersion in intensity levels in each box was found to be less than 2.4%, 2.0%, and 2.1% in the *B*-, *V*-, and *R*-band images, respectively; however, the dispersion in the median intensity levels was found to be 0.26%, 0.4%, and 0.19% in the *B*-, *V*-, and *R*-band images, respectively. We did not find any significant gradient in the median intensity levels in the source-free regions across any of the object images. The sky background level was determined as the mean of the median background intensity levels in each band separately. The background level, thus determined, was subtracted from the object image in each band. The regions covered by stars and dust were masked and excluded from the isophotal analysis. The deviant pixels with intensity values 3 σ below or above the mean intensity level were clipped, and the maximum accepted fraction of flagged pixels in an ellipse fitting was kept at 50%. The complex dust lanes and/or patches pass through the center of the galaxy, so it was not possible to determine the center very accurately. We choose the *R*-band image, which is the least affected by dust extinction, for detailed isophotal analysis. Starting with trial values of ellipticity (ϵ), position angle (θ), and ellipse center, an ellipse of mean intensity at a given length a of semimajor axis was fitted. The first two harmonics of the deviations from the trial ellipse were found. The best-fitted ellipses were determined after performing a minimum of 10 iterations and a maximum of 1000 iterations to minimize the deviations. The third and fourth harmonics of the residual intensity from the best-fitting ellipse were then evaluated. The procedure was repeated after changing the semimajor axis length by 10%, taking annuli and using the median value of the pixels for sampling along the elliptical path. The center was then determined by averaging the centers of the best-fitted ellipses. The center, thus determined, was kept fixed, and the above-described ellipse fitting procedure was repeated. The same center as determined for the *R*-band image was also used in the isophotal analysis of well-aligned images in other bands.

The generated radial distribution of surface brightness and isophotal shape parameter profiles are shown in Figure 3. The position angle profile reveals twisted isophotes. The ellipticity profile shows that the isophotes become progressively more elliptical in the outer regions. The parameters $a3$, $a4$ and $b3$, $b4$ are the amplitudes of sin 3θ, sin 4θ and cos 3θ, cos 4θ coefficients, respectively, of the isophotal deviation from the perfect ellipticity. It should be pointed out that in the inner regions ($a \leq 10''$) of NGC 4753, covered by

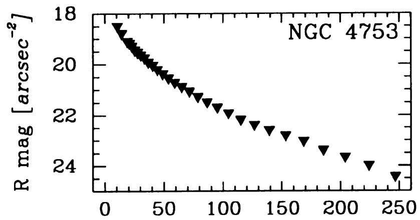

FIG. 3*a*

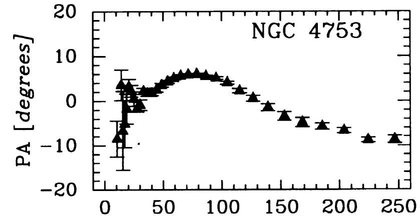

FIG 3*b*

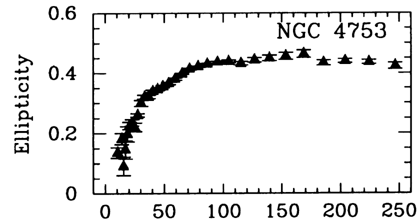

FIG. 3*c*

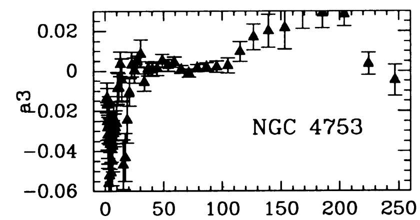

FIG. 3*d*

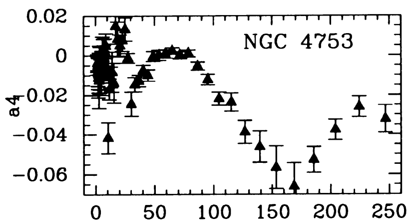

FIG. 3*e*

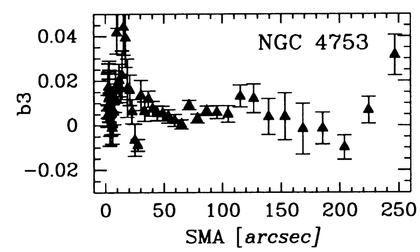

FIG. 3*f*

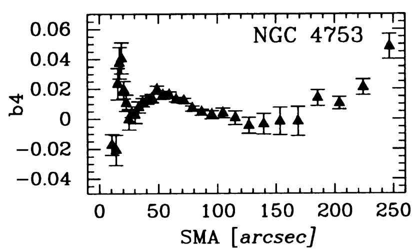

FIG. 3*g*

FIG. 3.—Results of *R*-band isophotal shape analysis of NGC 4753. (*a*) Surface brightness profile, (*b*) position angle profile, (*c*) ellipticity profile, (*d*) amplitude, *a*3, of residual sin 3θ coefficient of the isophotal deviation from perfect ellipse as a function of semimajor axis length (SMA), (*e*) amplitude, *a*4, of residual sin 4θ coefficient of the isophotal deviation from perfect ellipse as a function of SMA, (*f*) amplitude, *b*3, of residual cos 3θ coefficient of the isophotal deviation from perfect ellipse as a function *f* SMA, (*g*) amplitude, *b*4, of residual cos 4θ coefficient of the isophotal deviation from perfect ellipse as a function of SMA.

complex dust lanes and/or patches, more than 50% of the pixels are affected by dust extinction. The isophotal parameter profiles in the inner region, therefore, should not be taken very seriously. It has been tried to estimate the correct dust-free intensity by decreasing the accepted fraction of pixels to fit ellipses in the inner regions. This may have affected the actual shape parameters in the central regions. The core region of the galaxy of size of the order of the seeing disk was excluded from the isophotal analysis, as these are affected by the seeing.

3.3. *Color Index Maps*

We have generated color index maps ($B-R$, $B-V$, and $V-R$) using the broadband images to find out the distribution of dust. Instrumental colors were corrected for atmospheric extinction using the average extinction coefficients of Mayya (1991) and then converted into standard colors using the transformation coefficients given in Table 2. The $B-R$ color index map is shown in Figure 4, superposed on which are the contours of the Hα image (Singh et al. 1995). The brighter regions represent the part of the galaxy that are redder in color and hence represent cooler/dusty regions within the galaxy. The $B-R$ color in the dust-occupied regions within the galaxy was found to vary from 1.92 to 2.68. The maximum $B-R$ color is found to be 2.68 at the center. In the dust-free regions, the $B-R$ color as derived from the isophotal analysis was found to vary from 1.87 ± 0.07 at a semimajor axis length of 6″.0 to 1.38 ± 0.07 at the semimajor axis length of 246″.7. In the dust-free regions, the color gradient with respect to logarithmic Galactocentric radius *r*, $[d(B-R)/d(\log r)]$, was found to be -0.21 ± 0.05 for NGC 4753. This value can be compared with the color gradients $[d(B-R)/d(\log r)]$, -0.26, -0.23, and -0.14 for the S0 galaxies NGC 3414, NGC 3607, and NGC 5866, respectively, as derived by Vader et al. (1988). Hence, the average color gradient of NGC 4753 in the dust-free regions is normal for S0 galaxies. Figure 4 also suggests the coexistence of dusty regions with the Hα-emitting gas.

3.4. *Extinction Maps*

Several authors have studied dust properties of elliptical galaxies by an indirect method in which dust extinction is

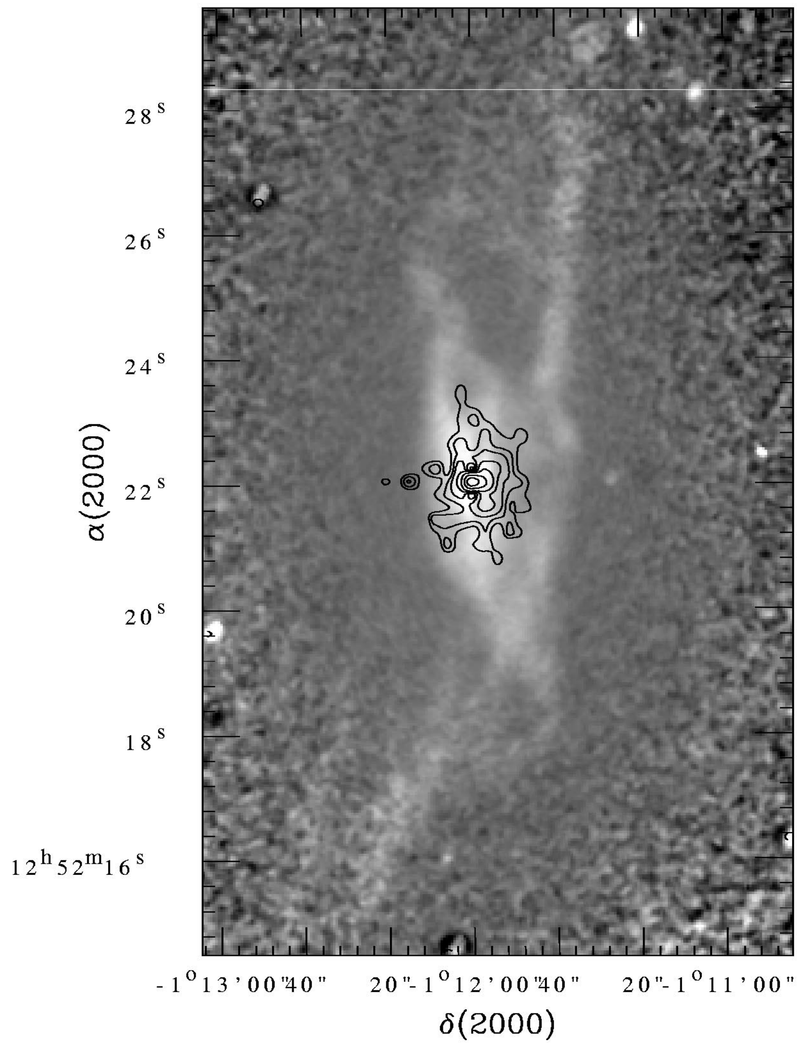

FIG. 4.—$B-R$ color image of NGC 4753, superposed on which are the contours of Hα image. The brighter regions represent part of the galaxy that are redder in color. The maximum $B-R$ color is found to be 2.677 at the center. The Hα + [N II] contours are drawn at levels 5%, 7.5%, 10%, 15%, 25%, 50%, and 80% of the peak intensity. The Hα + [N II] image is taken from Singh et al. (1995).

determined as a function of wavelength by comparing the actual distribution of intensity of the galaxy with that expected in the absence of dust extinction. The dust-free intensity distribution is modeled using elliptical isophotes. Sahu, Pandey, & Kambhavi (1998) have used the same method to study dust properties of an S0 galaxy, NGC 2076. The projections of three-dimensional intensity profiles of bulge and disk of an S0 galaxy onto the plane of sky are elliptical bulge and elliptical disk isophotes. If the disk is inclined with respect to the plane of the sky, disk isophotes are more elliptical than bulge isophotes. In many cases, the bulge and disk isophotal parameters are different. In the presence of a disk, the isophotes are not perfect ellipses. The deviations of isophotes of NGC 4753 from perfect ellipses are revealed by the presence of third- and fourth-order harmonics ($a3$, $b3$, $a3$, and $b4$). Therefore, the projected intensity distribution of bulge and disk can be modeled by using the isophotal parameters and the harmonics. The dust-free model images of NGC 4753 were generated by interpolating the fitted isophotal parameters (dust-free) with polynomial of order 3, including the third- and fourth-order harmonics determined above, thus incorporating the disklike structure. In order to check whether the dust-free intensity distribution of disk and bulge has been correctly modeled, we have carried out isophotal analysis of the dust-free model images of NGC 4753 and find that the profile of the parameter $b4$ derived from the isophotal analysis of dust-free "model image" of NGC 4753 is very similar to the profile of the parameter $b4$ derived from the isophotal analysis of the "observed image" of NGC 4753. Therefore, we conclude that the modeled dust-free intensity distribution of NGC 4753 has not been affected significantly by the presence of a stellar disk and the model image represents the actual dust-free intensity distribution of NGC 4753. The model images were used to create extinction maps in magnitude scale as follows:

$$A_\lambda = -2.5 \log (I_{\lambda,\mathrm{obs}}/I_{\lambda,\mathrm{model}}) , \qquad (5)$$

where $\lambda = B, V, R$. Note that absolute flux calibration is not needed for this purpose. The extinction map of NGC 4753 in the B band is shown in Figure 5. The brighter areas within the galaxy represent regions of large optical depth associated with the dust extinction. The extinction in the B band was found to vary from 0.881 ± 0.036 to 0.438 ± 0.058. This estimate excludes central regions ($a \le 10''$) because of the poor accuracy of the ellipse-fitting

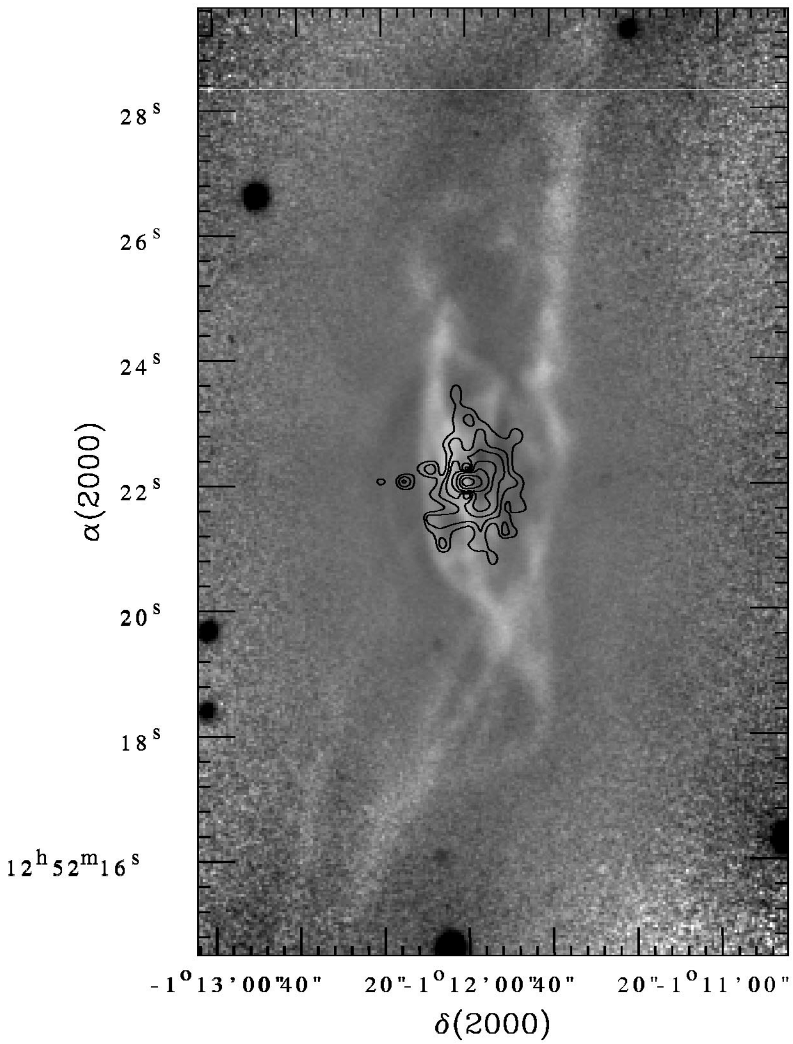

FIG. 5.—Extinction image of NGC 4753 in the B band. The brighter areas represent regions of large optical depth associated with the dust extinction. The superposed contours of the Hα + [N II] (Singh et al. 1995) map are drawn at levels 5%, 7.5%, 10%, 15%, 25%, 50%, and 80% of the peak intensity and show spatial association of dust and Hα gas.

procedure. Figure 5 also shows overlapped contours of Hα image, which demonstrates that Hα-emitting regions and dust-occupied regions are cospatial. The extinction maps in different bands were used to study the dust properties, as described in the next section.

3.5. *Extinction Curve*

To quantify the extinction due to dust, we selected regions in the extinction map obviously occupied by dust. The numerical values of extinction, A_λ ($\lambda = B, V, R$), were calculated as the mean extinction within square boxes of size 5×5 pixels, which is comparable to the size of the seeing disk. The uncertainties associated with the derived extinction values were estimated from the pixel-to-pixel scatter within each box. Because the isophotal model fits were mostly unreliable in the central regions ($a \leq 10''$), we considered it safer to exclude these regions from the estimation of extinction values. The average extinction values over the dust-occupied regions ($a \geq 10''$) within the galaxy image were assigned to the dust-occupied central regions. Because the contribution from Hα and [N II] line emission to the R band are mostly concentrated in the central regions ($a \leq 10''$) of NGC 4753, the derived extinction values in R band are not significantly affected by the presence of line emission.

To determine the ratio of total extinction to selective extinction, we fitted bivariate correlated measurement errors and intrinsic scatter (BCES) least-squares regression lines between different extinction values. The BCES method is a direct generalization of the ordinary least-squares (OLS) regression method, modified to accommodate the measurement errors either correlated or uncorrelated and intrinsic scatter (for details, see Akritas, Bershady, & Bird 1996). In the presence of errors, the use of the OLS regression method can cause considerable bias, as it does not take into account measurement errors in the variables. Apart from the measurement errors in the derived extinction values, there is also intrinsic scatter depending on spatial distribution of dust and their properties. The measurement errors for extinction in two bands are uncorrelated. As a consequence, we must use the BCES technique, ignoring the correlated errors, to derive the linear regression lines relating extinction in two bands. We fitted the BCES regression lines A_y on A_x and A_x on A_y ($x, y = B, V, R$; $x \neq y$). The bisector

TABLE 3

BCES and OLS Linear Regression Coefficients

Fit	Slope	Intercept
BCES($A_B \mid A_V$)	2.61 ± 0.476	− 0.292 ± 0.102
OLS($A_B \mid A_V$)........	1.20 ± 0.046	0.009 ± 0.011
BCES($A_V \mid A_B$)	0.747 ± 0.113	0.106 ± 0.0255
OLS($A_V \mid A_B$)........	1.323 ± 0.054	− 0.017 ± 0.013
BCES bisector......	1.32 ± 0.0881	− 0.0168 ± 0.0197
OLS bisector	1.26 ± 0.048	− 0.003 ± 0.012
BCES($A_R \mid A_V$)	2.10 ± 0.493	− 0.315 ± 0.110
BCES($A_V \mid A_R$)	0.188 ± 0.131	0.112 ± 0.0294
BCES bisector......	0.77 ± 0.0811	− 0.0182 ± 0.0184
BCES($A_B \mid A_R$)	4.53 ± 2.08	− 0.404 ± 0.314
BCES($A_R \mid A_B$)	0.852 ± 0.146	0.0221 ± 0.0254
BCES bisector......	1.66 ± 0.171	0.143 ± 0.023

of these two regression lines was chosen as the best-fit line. The bisector treats the variables symmetrically and has been recommended for scientific problems where the goal is to estimate the underlying functional relationship between the variables (see Isobe et al. 1990; Feigelson & Babu 1992). To compare our results and to see the effects of errors on the regression coefficients, we have also fitted OLS regression lines using the method described by Isobe et al. (1990) between extinction values in different bands. The BCES and OLS regression coefficients are given in Table 3, and the fitted straight lines are shown in Figures 6*a*–6*d*. In Figure 6*a*, the lines marked as 1, 2, and 3 are the linear regression fits of A_B on A_V, A_V on A_B, and the bisector of the two lines, respectively, derived using the BCES technique. In Figure 6*b*, lines 1, 2, and 3 are same as those in Figure 6*a* but derived using the OLS method. As can be seen in Table 3, the lines marked 1 in Figures 6*a* and 6*b* are significantly different. It is also seen in Table 3 that the lines marked 2 in Figures 6*a* and 6*b* are significantly different, but the BCES bisector and OLS bisector lines marked 3 in Figures 6*a* and 6*b* are similar. The difference in lines 1 in Figures 6*a* and 6*b* and the difference in lines 2 can be explained as the effect of large errors as shown in Figure 6*a*. The BCES bisector and OLS bisector yielded intercepts close to zero, which are within 1 standard deviation, as expected. This further suggested the validity of use of the bisector line between extinction values in different bands. Henceforth, we use the BCES bisector line as the best-fit regression line. The linear regression fit between A_R and A_B using the BCES bisector method is shown in Figure 6*c*. Similarly, the BCES bisector line of A_V and A_R is shown in Figure 6*d*.

The best-fitting BCES bisector slopes and their associated uncertainties were subsequently used to derive the ratio of total extinction to selective extinction, $R_\lambda = (A_\lambda/A_B - A_V)$, and their associated uncertainties. The average extinction curve for the areas occupied by dust in NGC 4753 is shown in Figure 7, along with the extinction curve of our Galaxy for comparison. The total extinction to selective extinction values for the Milky Way were derived in the same manner as for NGC 4753 from the ratios of extinction that, for the Galaxy, were taken from Rieke & Lebofsky (1985). Figure 7 shows that the ratio $R_\lambda = A_\lambda/(A_B - A_V)$ varies linearly with inverse wavelength, which is consistent with the result that for small grain size $x < 1$, $Q_{\rm ext} \propto \lambda^{-1}$, where $x = (2\pi a/\lambda)$, a is the grain radius, and $Q_{\rm ext}$ is the

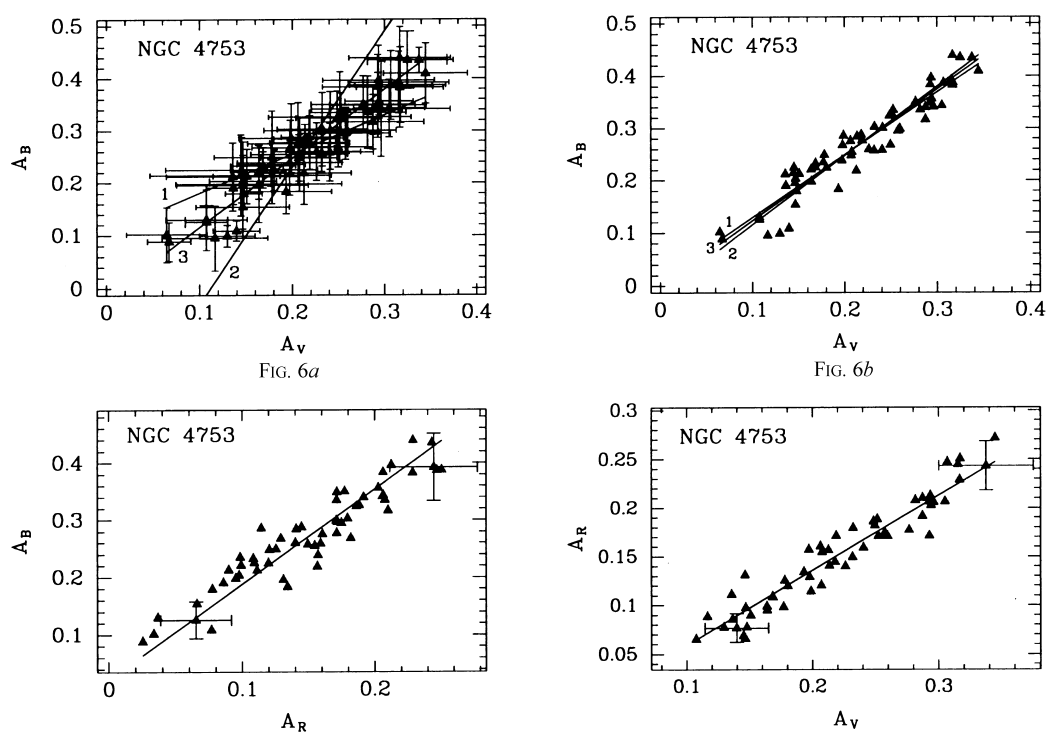

FIG. 6*a* FIG. 6*b* FIG. 6*c* FIG. 6*d*

FIG. 6.—BCES and OLS regression lines between extinction values in different passbands. (*a*) BCES regression lines between extinction in V and B bands. Line 1 is the BCES regression line of A_V on A_B, line 2 is the BCES regression line of A_B on A_V, and line 3 represents the BCES bisector of lines 1 and 2. (*b*) OLS regression lines between A_V on A_B. Line 1 is the OLS line of A_V on A_B, line 2 is the OLS line of A_B on A_V, and line 3 is the OLS bisector of lines 1 and 2. (*c*) BCES bisector regression line of A_R and A_V. (*d*) BCES bisector regression line of A_R and A_B. The quantities of A_λ ($\lambda = B$, V, and R) represent the dust extinction in the λ-band.

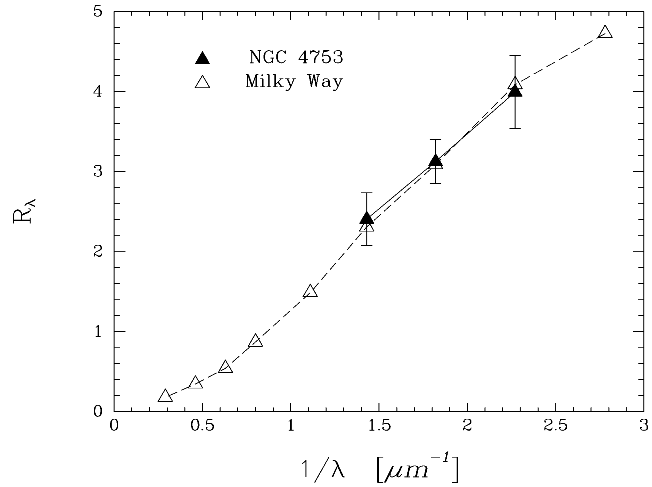

FIG. 7.—Extinction curve of NGC 4753. The Galactic extinction curve is also plotted for comparison. The quantity R_λ [$= A_\lambda/(A_B - A_V)$] is the ratio of total extinction to selective extinction in the band $\lambda = B, V, R$.

extinction efficiency. From Figure 7 it is obvious that the extinction curve for NGC 4753 is very similar to the Galactic extinction curve in the visible region. Also, the ratio of total extinction to selective extinction, $R_V = 3.1 \pm 0.3$ for NGC 4753, is similar to the Galactic value of 3.1. The extinction curves in Figure 7 imply that the grain size distribution within the dusty regions of NGC 4753 is similar to that of our Galaxy. This conclusion about the grain size distribution can be used to determine the total dust mass within NGC 4753, as discussed below.

3.6. *Dust Mass from Optical Extinction*

We have used the method of Goudfrooij et al. (1994c) to derive the dust mass from optical extinction values. The total dust mass can be estimated by integrating the dust column density, given by

$$\Sigma_d = \int_{a_{\min}}^{a_{\max}} \frac{4}{3} \pi a^3 \rho_d n(a) da \times l_d \tag{6}$$

over the dust-occupied areas. In equation (6), ρ_d is the grain mass density, $n(a)$ is the grain size distribution function, and $a_{\min}$ and $a_{\max}$ are the lower and upper cutoffs of the grain size distribution. The dust column length, l_d, along the line of sight is determined from

$$A_\lambda = 1.086 C_{\text{ext}}(\lambda) \times l_d , \tag{7}$$

where A_λ is extinction in magnitude at wavelength λ and $C_{\text{ext}}(\lambda)$ is the extinction cross section of spherical grains per unit volume. $C_{\text{ext}}(\lambda)$ can be written as

$$C_{\text{ext}}(\lambda) = \int_{a_{\min}}^{a_{\max}} Q_{\text{ext}}(a, \lambda) \pi a^2 n(a) da , \tag{8}$$

where $Q_{\text{ext}}(a, \lambda)$ is the extinction efficiency of grains of radii a at wavelength λ. In computing $C_{\text{ext}}(\lambda)$, the contribution of different chemical compositions of the dust grains is taken into account.

Because the extinction curve of NGC 4753 is quite similar to that of our Galaxy, we have employed the grain size distribution of Mathis, Rumpl, & Nordsieck (1977), that is,

$$n(a)da = A_i n_{\text{H}} a^{-3.5} da \quad (a_{\min} \le a \le a_{\max}) ,$$

with $a_{\min} = 0.005$ and $a_{\max} = 0.22$ μm in the case that $R_V = 3.1$. In the above equation, n_{H} is the number density of H nuclei, and A_i is the abundance of grains of type i per H atom. As to the composition of grains, we assume spherical grains that are composed of either graphite or silicates, with equal abundances. This is justified by the fact that the Galactic extinction curve can be fitted assuming the above composition (Mathis et al. 1977). We have used parameterized V-band extinction efficiencies of Goudfrooij et al. (1994c) for the two types of grains. The adopted values are

$$Q_{\text{ext,silicate}} = \begin{cases} 0.8a/a_{\text{silicate}} , & \text{for } a < a_{\text{silicate}} , \\ 0.8 , & \text{for } a \ge a_{\text{silicate}} , \end{cases}$$

$$Q_{\text{ext,graphite}} = \begin{cases} 2.0a/a_{\text{graphite}} , & \text{for } a < a_{\text{graphite}} , \\ 0.8 , & \text{for } a \ge a_{\text{graphite}} , \end{cases}$$

with $a_{\text{silicate}} = 0.1$ and $a_{\text{silicate}} = 0.05$ μm. The values of various parameters used for estimation of total dust mass are given in Table 4. The average dust mass per pixel was computed using equations (6)–(9) and the average value of A_V. We have adopted a distance of 8.7 Mpc for NGC 4753 (see Table 1). To find the total dust mass of NGC 4753, we integrated the average dust mass per pixel over all the dust-occupied pixels, which were determined based on the criterion that a pixel within the galaxy image is considered to be dusty if the pixel value in the ratio of observed and smooth model image is 2 σ or more below unity. The total mass of dust within NGC 4753, calculated thus, is 1.5×10^5 $M_\odot$. The mass of dust can also be determined based on FIR emission, as discussed in the next section.

3.7. *IRAS Properties*

NGC 4753 was detected as a point source in the *IRAS* survey at all four bands: 12, 25, 60, and 100 μm. We obtained *IRAS* flux densities from Knapp et al. (1989). The flux densities at 60 and 100 μm were corrected for the contribution of circumstellar dust emission (Goudfrooij & de Jong 1995). The dust temperature was determined to be 30.4 K on the basis of the ratio of flux densities at 100 and 60 μm under the assumption that the FIR emission from the dust grains within NGC 4753 is governed by an emissivity law where emissivity is proportional to λ^{-1} at wavelengths $\lesssim$ 200 μm (Schwartz 1982; Hildebrand 1983; Kwan & Xie 1992). Because a distribution of temperature may be more appropriate for dust, the derived dust temperature should be regarded as a representative value. We have estimated the dust mass of NGC 4753 following the method outlined in Hildebrand (1983), Thronson & Telesco (1986), and Goudfrooij & de Jong (1995), which is based on measurements of FIR flux density $f(\nu)$, dust temperature T_d, dust

TABLE 4

PARAMETERS USED IN THE ESTIMATION OF DUST MASS

Parameter	Value	Reference
A_{silicate}	$10^{-25.11}$ cm$^{2.5}$/H	1
A_{graphite}	$10^{-25.16}$ cm$^{-2.5}$/H	1
n_{H}	20 cm^{-3}	2
$\rho_{d,\text{graphite}}$	3.26 g cm^{-3}	1
$\rho_{d,\text{silicate}}$	3.3 g cm^{-3}	1

REFERENCES.—(1) Draine & Lee 1984; (2) Hoyle & Wickramasinghe 1991.

emissivity $Q(\nu)$, and size of the grains. The total dust mass is given by

$$M_d = \frac{D^2 f(\nu)}{B(\nu, T_d)} \times \frac{(4/3)a}{Q(\nu)} \rho_d , \tag{9}$$

where ρ_d is the specific grain mass density, a is the average grain radius weighted by the grain volume, and D is the distance of the galaxy. The derived cool dust mass is $3.46 \times 10^5\ M_\odot$. Assuming that the IR spectrum of NGC 4753 can be fitted by a function of the form $f(\nu) \propto \nu B(\nu, T_d)$, which is a good approximation to the total IR spectrum of most galaxies (Telesco & Harper 1980; Rickard & Harvey 1984), the total IR luminosity can be written as

$$L_{\rm IR}(L_\odot) = 3.7 \times 10^{-12} D^2 f(\nu) T_d^5 \lambda^4 \times [\exp(1.44 \times 10^4/\lambda T) - 1] \tag{10}$$

(Thronson & Telesco 1986), where D is the object distance in megaparsecs, the flux density $f(\nu)$ is in janskys, and λ is in micrometers. Using the above relation the total IR luminosity of NGC 4753 is estimated to be $6.6 \times 10^8\ L_\odot$.

4. DISCUSSION

The surface brightness profile and isophotal shape parameters (Fig. 3) of NGC 4753 reveal some intensity features of this early-type galaxy. The parameter $b4$, the amplitude of the cos 4θ coefficient of the isophotal deviation from the best-fitting ellipse, is interpreted as being due to an embedded disk ($b4 > 0$) or boxiness of isophotes ($b4 < 0$; e.g., Peletier et al. 1990). The positive values of $b4$ indicate a disk component in NGC 4753. The galaxy is very flattened in its outer parts. The presence of disk component is supported by large rotational velocities, $v \geq 250$ km s^{-1}, measured by Chromey (1973). The disk component and twisted isophotes as revealed by the position angle profile, Figure 3*b*, are supported by a model where an inclined disk twisted by differential precession fits the observed dust lanes lying very well on the disk (Steiman-Cameron et al. 1992).

We have derived the dust mass of NGC 4753 from optical extinction as well as from *IRAS* flux densities. The ratio of the two dust masses, $M_{d,\rm IRAS}/M_{d,\rm optical}$, is 2.28. The discrepancy can be attributed to the fact that the dust mass derived from optical extinction is a lower limit because the extinction is observed only when the dust is in front of the stars. The dust is probably distributed between the stars or stellar system, and the actual dust mass is expected to be higher than the dust mass derived from optical extinction. Goudfrooij & de Jong (1995) have reported that the average ratio $\langle M_{d,\rm IRAS}/M_{d,\rm optical} \rangle$ to be 8.4 ± 1.3 for a large sample of elliptical galaxies for which the presence of dust is revealed by both FIR emission and optical dust lanes or patches. This ratio is significantly higher than the ratio for NGC 4753, which implies that the dust-mass discrepancy in NGC 4753 is not as severe as for an average elliptical galaxy. Sahu et al. (1998) have reported that $M_{d,\rm IRAS}/M_{d,\rm optical} = 1.14$ for an S0 galaxy, NGC 2076. This indicates that the difference in dust mass derived from FIR emission and optical extinction is not significant for S0 galaxies, in contrast to the dust-mass discrepancy in elliptical galaxies. This is an expected result, because the dust masses derived for spiral galaxies from optical and *IRAS* data reveal that $M_{d,\rm IRAS} \ll M_{d,\rm optical}$ (Goudfrooij 1996) and the S0 galaxies, being intermediate in the morphological sequence from ellipticals to spirals, can be expected to have intermediate properties.

A rough estimate of molecular gas content of NGC 4753 can be made from the dust mass derived from FIR flux if we assume that the ratio of molecular gas to dust mass is in the range 50–700, as given by Wiklind, Combes, & Henkel (1995) for emission-line regions. This would render the molecular gas mass of NGC 4753 in the range (0.2–2.4) $\times 10^8\ M_\odot$. The masses of different contents of NGC 4753 are given in Table 5.

The origin of the observed interstellar dust can be either internal (e.g., due to mass loss from stars) or external (galaxy-galaxy interaction or merger). In the solar neighborhood, the potential sources of dust grains are supernovae, red giant stars, protostellar nebulae, and planetary nebulae with relative weights of 100, 37, less than 16, and 6, respectively (Dwek & Scalo 1980). In the case of early-type galaxies, the rate of star formation and hence the rate of supernova explosions are much lower than the corresponding rates in spiral galaxies. The rate of supernova explosions in early-type galaxies is about a factor of 16 smaller then the rate in spiral galaxies (Sbc–Sd; Cappellaro et al. 1993). Therefore, it can be expected that the dominant sources of dust grains in early-type galaxies are the red giant stars. In the following, we consider dust mass within NGC 4753 arising from red giant stars and neglect the other possible sources of dust grains. The total mass-loss rate from red giant stars within NGC 4753 can be estimated from the excess IR luminosity arising from circumstellar shells of the red giant stars (see Soifer et al. 1986). The excess IR luminosity arising from circumstellar shells of red giant stars can be determined by comparing the IR luminosities from photospheres of normal stars and red giant stars and by counting the total number of red giant stars within NGC 4753. Because individual stars within NGC 4753 could not be resolved, it is not possible to determine the excess IR luminosity arising from circumstellar shells of the red giant stars. Hence, the total mass-loss rate from red giant stars within NGC 4753 cannot be determined directly. However, following the analysis of Jura et al. (1987) and assuming that stellar population within NGC 4753 is similar to that of elliptical galaxies or bulge of M31, the total mass-loss rate from red giant stars within NGC 4753 can be estimated. The total mass-loss rate from red giant stars within an elliptical galaxy can be written as (Jura et al. 1987)

$$\dot{M}\ (M_\odot\ {\rm yr}^{-1}) = 4.3 \times 10^{-30} L_\nu(12\ \mu{\rm m})\ ({\rm ergs\ s^{-1}\ Hz^{-1}}) , \tag{11}$$

where L_ν (12 μm) is the luminosity per unit frequency at 12 μm. For NGC 4753, we calculate $L_\nu(12\ \mu{\rm m})$ to be 3.0×10^{26}

TABLE 5

MASSES OF DIFFERENT COMPONENTS OF ISM IN NGC 4753

Component	Mass ($M_\odot$)
Dust ($M_{d,\rm optical}$)[a]	1.5×10^5
Dust ($M_{d,\rm IRAS}$)[a]	3.46×10^5
H I[b]	$\leq 5.28 \times 10^8$
Molecular gas[a]	$0.2–2.4 \times 10^8$
Hα gas[c]	0.67×10^5

[a] Derived value.

[b] Based on 21 cm line emission observed by Knapp et al. 1985.

[c] Taken from Singh et al. 1995.

ergs s^{-1} Hz^{-1} from the measured flux at 12 μm and adopting a distance of 8.7 Mpc (see Table 1). Substituting L_ν (12 μm) into the above equation, we estimate the total mass-loss rate from red giant stars within NGC 4753 to be 1.3×10^{-3} $M_\odot$ yr^{-1}. The derived mass-loss rate is uncertain because stellar population within elliptical galaxies and NGC 4753 may be significantly different; however, the mass-loss rate is not expected to vary by large factors. If we assume that the gas-to-dust ratio in the circumstellar shells of red giant stars to be 100:1 by mass, with a factor of 2–3 uncertainty (see Knapp, Sandell, & Robson 1993), the total loss rate of dust mass by red giant stars within NGC 4753 is about 1.3×10^{-5} $M_\odot$ yr^{-1}. The mass of dust accumulated within NGC 4753 can be estimated by the mass loss from stars and by the mechanisms of destruction of dust (see below). The rate at which dust mass is accumulated within NGC 4753 can be written as

$$\frac{\partial M_d(t)}{\partial t} = \frac{\partial M_{d,s}}{\partial t} - M_d(t)\tau^{-1} , \qquad (12)$$

where $(\partial M_{d,s}/\partial t)$ is the loss rate of mass in the form of dust by red giant stars and τ^{-1} is the destruction rate of dust. The second term on the right represents the rate at which mass of dust within NGC 4753 is destroyed. Assuming that the mass loss from red giant stars begins at an age $\sim 10^6$ yr of NGC 4753 and taking $\tau^{-1} \sim 7.14 \times 10^{-10}$ yr^{-1} (see below), we have solved numerically the above equation for the mass of dust accumulated as a function of time. The buildup of mass of dust within NGC 4753 is shown in Figure 8. Assuming an age of 10^{10} yr for NGC 4753, the total mass of dust accumulated within NGC 4753 is calculated to be 1.8×10^4 $M_\odot$, which is about a factor of 10 lower than the measured mass of dust. This indicates that the mass-loss rate from red giant stars is probably not sufficient to account for the observed dust within NGC 4753. Based on our simplified calculation given above, the possibility of an external origin of dust within NGC 4753 cannot be ruled out.

X-ray emission of varying amounts is seen in several early-type galaxies. Integrated X-ray emission from discrete sources and the presence of hot gas ($\sim 10^7$ K) can both contribute to the overall X-ray emission. Hot plasma, if present, can destroy the dust very efficiently (Draine & Salpeter 1979a). The ratio of total X-ray luminosity to absolute blue luminosity is a good indicator of the presence of hot gas in an early-type galaxy (Canizares et al. 1987). Therefore, to estimate the dust destruction timescale, we examine X-ray emission from NGC 4753. The quantity log (L_X/L_B) (L_X in ergs s^{-1} and L_B in $L_\odot$) for NGC 4753 is 29.42, based on which Canizares et al. (1987) would conclude that the total X-ray luminosity of NGC 4753 is consistent with that expected from the integrated X-ray luminosity of discrete sources. The galaxy NGC 4753 is a member of the lowest (L_X/L_B) group in Kim, Fabbiano, & Trinchieri (1992), where it has been shown that early-type galaxies in the lowest (L_X/L_B) group have a very soft X-ray excess that amounts to about half the total X-ray emission. This emission could be due either to a cooler ISM or to the integrated emission of soft stellar sources. In any case, ISM of these galaxies is not heated to high X-ray temperatures. This implies that the dust in NGC 4753 is unlikely to be embedded in a very hot plasma. In the absence of hot plasma, the most effective destruction mechanism for refractive grains (e.g., graphite and silicate) are sputtering and grain-grain collisions in low-velocity shocks ($v_{shock} \leq 60$ km s^{-1}) and sputtering in supernova-driven blast waves (Goudfrooij et al. 1994c). Using the model of Draine & Salpeter (1979b), appropriate for X-ray faint early-type galaxies, and a recent estimate for the rate of supernova explosions in early-type galaxies, Goudfrooij et al. (1994c) have estimated the lifetime $\tau \sim 1.4 \times 10^9$ yr for 0.1 μm refractory grains. We have used this value to calculate the mass of dust accumulated within NGC 4753, given above.

Hα + [N II] emission-line regions in the center of NGC 4753 are embedded in the regions with substantial optical extinction (see Figs. 4 and 5). This association of emission-line regions and regions with substantial dust absorption points toward the coexistence of dust and warm gas ($\sim 10^4$ K) within NGC 4753. The observed Hα line emission can be accounted by photoionization from post–asymptotic giant branch stars (see Singh et al. 1994, 1995), which can also supply significant amounts of dust.

As to the fate of cool dust and gas, we examine the possibility of star formation within NGC 4753. The galaxy occupies an intermediate position but close to the lower right end in the phenomenological *IRAS* color-color diagram of Helou (1986), where both the cirrus component and active star-forming regions contribute to the total FIR emission. However, the FIR emission from active star-forming regions is less than 50% of the total FIR luminosity, so that the total FIR emission of NGC 4753 cannot be interpreted as due to current star formation. Following Thronson & Telesco (1980), the current star formation rate averaged over past 2×10^6 yr can be calculated using the relation

$$\dot{M}_{FIR} = 6.5 \times 10^{-10} L_{FIR}(L_\odot) , \qquad (13)$$

where L_{FIR} is the total FIR luminosity. However, considering the phenomenological model of Helou (1986), only the FIR luminosity due to the active star-forming regions must be used in above expression. We estimate the current star formation rate of NGC 4753, averaged over past 2×10^6 yr, to be less than 0.21 $M_\odot$ yr^{-1}. As discussed above, the cirrus component of dust contributes more than 50% to the total FIR luminosity, hence significant amount of dust within NGC 4753 is in the form of cirrus. This suggests that the

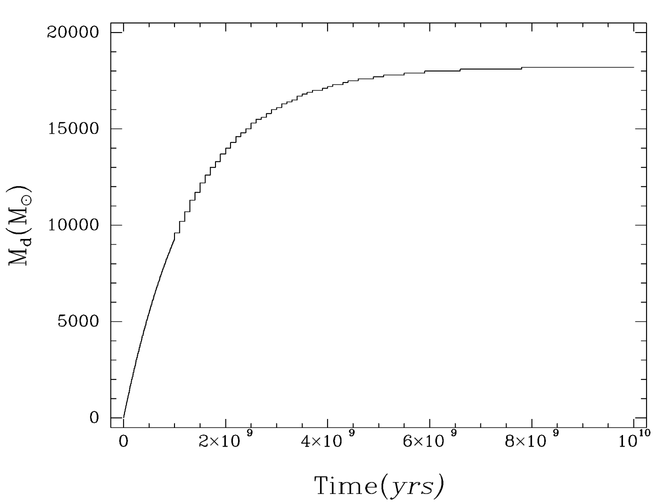

FIG. 8.—Total dust mass accumulated within NGC 4753 as a function of time.

cirrus clouds are not destroyed efficiently because of the lack of hot ISM. Also, these regions are not sufficiently dense to lead to gravitational instability to form stars.

5. CONCLUSIONS

Our isophotal analysis of NGC 4753 has revealed a twisted disk component in it. The dust grain properties of NGC 4753 appear to be similar to that of our Galaxy, based on comparison of the extinction curves. The derived mass of cold dust in NGC 4753 is $1.5 \times 10^5\ M_{\odot}$ of NGC 4753 based on optical extinction and $3.46 \times 10^5\ M_{\odot}$ based on FIR fluxes. The discrepancy between the two dust masses for NGC 4753 is not as severe as the discrepancy generally found for the elliptical galaxies. The accumulated mass of dust within NGC 4753 from mass loss by red giant stars after taking into account the efficient destruction processes is $\sim 1.8 \times 10^4\ M_{\odot}$, which is about a factor of 10 lower than the measured dust mass. Dust and ionized gas coexist within NGC 4753. The current star formation rate of NGC 4753, averaged over past 2×10^6 yr, is derived to be less than 0.21 $M_{\odot}$ yr^{-1} using the FIR emission arising from active star-forming regions. A significant amount of dust within NGC 4753 seems to exist in the form of cirrus.

We thank the director of the Indian Institute of Astrophysics and the Time Allocation Committee for allotting the dark nights for our observations. The members of the technical support staff of the VBT are gratefully acknowledged for their assistance during the observations. We thank an anonymous referee, whose critical comments and suggestions helped in improving the paper. We also thank A. D. Karnik and D. K. Ojha for helpful discussions during the analysis. This research has made use of the NASA/IPAC Extragalactic Database, which is operated by the Jet Propulsion Laboratory, Caltech, under contract with the National Aeronautics and Space Administration.

REFERENCES

Akritas, M. G., Bershady, M. A., & Bird, C. M. 1996, ApJ, 470, 706
Anupama, G. C., Kembhavi, A. K., Prabhu, T. P., Singh, K. P., & Bhat, P. N. 1994, A&AS, 103, 315
Bertola, F., Galleta, G., Kotanyi, C., & Zeilinger, W. W. 1988, MNRAS, 234, 733
Bhat, P. N., Singh, K. P., Prabhu, T. P., & Kembhavi, A. K. 1992, J. Astrophys. Astron., 13, 293
Buta, R. J., et al. 1985, PASP, 97, 229
Caldwell, N. 1984, ApJ, 278, 96
Canizares, C. R., Fabbiano, G., & Trinchieri, G. 1987, ApJ, 312, 503
Cappellaro, E., Turatto, M., Benetti, S., Tsvetkov, D. Yu., Bartunov, O. S., & Makarova, I. N. 1993, A&A, 273, 383
Chevalier, C., & Ilovaisky, S. A. 1991, A&AS, 90, 225
Chromey, F. R. 1973, A&A, 29, 77
de Jong, T., Nørgaard-Nielsen, H. U., Hansen, L., & Jørgensen, H. E. 1990, A&A, 232, 317
de Vaucouleurs, G., de Vaucouleurs, A., Corwin, H. G., Jr., Buta, R. J., Paturel, G., & Fouqué, P. 1991, The Third Reference Catalogue of Bright Galaxies (New York: Springer) (RC3)
Draine, B. T., & Lee, H. M. 1984, ApJ, 285, 89
Draine, B. T., & Salpeter, E. 1979a, ApJ, 231, 77
———. 1979b, ApJ, 231, 438
Dwek, E., & Scalo, J. M. 1980, ApJ, 239, 193
Ebneter, K., Djorgovski, S., & Davis, M. 1988, AJ, 95, 422
Fabbiano, G., Kim, D. W., & Trinchieri, G. 1992, ApJS, 80, 531
Fabian, A. C., & Thomas P. A. 1987, in IAU Symp. 127, Structure and Dynamics of Elliptical Galaxies, ed. P. T. de Zeeuw (Dordrecht: Reidel), 155
Feigelson, E. D., & Babu, G. J. 1992, ApJ, 397, 55
Forman, W., Jones, C., & Tucker, W. 1985, ApJ, 293, 102
Goudfrooij, P. 1996, in Proc. New Extragalactic Perspectives in the New South Africa: Changing Perceptions of the Morphology, Dust Content and Dust-Gas Ratios in Galaxies, ed. D. L. Block (Dordrecht: Kluwer), in press
Goudfrooij, P., & de Jong, T. 1995, A&A, 298, 784
Goudfrooij, P., de Jong, T., Nørgaard-Nielsen, H. U., & Hansen, L. 1994c, MNRAS, 271, 833
Goudfrooij, P., Hansen, L., Jørgensen, H. E., & Nørgaard-Nielsen, H. U. 1994b, A&AS, 105, 341
Goudfrooij, P., Hansen, L., Jørgensen, H. E., Nørgaard-Nielsen, H. U., de Jong, T., & van den Hock, L. B. 1994a, A&AS, 104, 179
Habe, A., & Ikeeuchi, S. 1985, ApJ, 289, 540
———. 1988, ApJ, 326, 84
Hawarden, T. G., Elson, R. A. W., Longmore, A. J., Tritton, S. B., & Corwin, H. G. 1981, MNRAS, 196, 747
Helou, G. 1986, ApJ, 311, L33
Hildebrand, R. D. 1983, QJRAS, 24, 267
Hoyle, F., & Wickramasinghe, N. C. 1991, in The Theory of Cosmic Grains (Dordrecht: Kluwer), 94
Isobe, T., Feigelson, E. D., Akritas, M. G., & Babu, G. J. 1990, ApJ, 364, 104
Jaffe, W., Ford, H. C., O'Cornell, R. W., van den Bosch, F. C., & Ferrarese, L. 1994, AJ, 108, 1567
Jedrzejewski, R. I. 1987, MNRAS, 226, 747
Jura, M. 1986, ApJ, 306, 483
Jura, M., Kim, D. W., Knapp, G. R., & Guhathakurta, P. 1987, ApJ, 312, L11
Kim, D. -W., Fabbiano, G., & Trinchieri, G. 1992, ApJ, 393, 134
Knapp, G. R., Guhathakurta, P., Kim, D. W., & Jura, M. 1989, ApJS, 70, 329
Knapp, G. R., Sandell, G., & Robson, E. I. 1993, ApJS, 88, 173
Knapp, G. R., Turner, E. L., & Cunniffer, P. E. 1985, AJ, 90, 454
Kwan, J., & Xie, S. 1992, ApJ, 398, 105
Mathis, J. S., Rumpl W., & Nordsieck, K. H. 1977, ApJ, 217, 45
Mayya, Y. D. 1991, J. Astrophys. Astron., 12, 319
Merritt, D., & de Zeeuw, P. T. 1983, ApJ, 267, L19
Peletier, R. F., Davies, R. L., Illingworth, G. D., Davis, L. E., & Cawson, M. 1990, AJ, 100, 1091
Phillips, M. M., Jenkins, C. R., Dopita, M. A., Sadler, E. M., & Binette, L. 1986, AJ, 91, 1062
Rickard, L. J., & Harvey, P. M. 1984, AJ, 89, 1520
Rieke, G. H., & Lebofsky, M. J. 1985, ApJ, 288, 618
Sadler, E. M., & Gerhard, O. E. 1985, MNRAS, 214, 177
Sahu, D. K., Pandey, S. K., & Kembhavi, A. 1998, A&A, 333, 803
Sandage, A. 1961, The Hubble Atlas (Washington: Carnegie Inst. Washington)
Schwartz, P. R. 1982, ApJ, 252, 589
Singh, K. P., Bhat, P. N., Prabhu, T. P., & Kembhavi, A. K. 1995, A&A, 302, 658
Singh, K. P., Prabhu, T. P., Kembhavi, A. K., & Bhat, P. N. 1994, ApJ, 424, 638
Soifer, B. T., Rice, W. L., Mould, J. R., Gillet, F. C., Rowan-Robinson, M., & Habing, H. J. 1986, ApJ, 304, 651
Steiman-Cameron, T. Y., Kormendy, J., & Durisen, R. H. 1991, AJ, 104, 1339
Stetson, P. B. 1987, PASP, 99, 191
Telesco, C. M., & Harper, D. A. 1980, ApJ, 235, 392
Thronson, H., & Telesco, C. 1986, ApJ, 311, 98
Vader, J. P., Vigroux, L., Lachieze-Rey, M., & Souviron, J. 1988, A&A, 203, 217
Van Dokkum, P. G., & Franx, M. 1995, AJ, 110, 2027
Wiklind, T., Combes, F., & Henkel, C. 1995, A&A, 297, 643
Wiklind, T., & Rydbeck, G. 1986, A&A, 164, L22